

REF ID: A6131
LIST
ARL Call No. 82096
Copy No. 1 of 2 cysm

Semiannual Technical Summary

Integrated Optical Circuits

30 June 1974

Prepared for the Advanced Research Projects Agency
under Electronic Systems Division Contract F19628-73-C-0002 by

Lincoln Laboratory

MASSACHUSETTS INSTITUTE OF TECHNOLOGY
LEXINGTON, MASSACHUSETTS



Approved for public release; distribution unlimited.

ADA006813

The work reported in this document was performed at Lincoln Laboratory, a center for research operated by Massachusetts Institute of Technology. This work was sponsored by the Advanced Research Projects Agency of the Department of Defense under Air Force Contract F19628-73-C-0002 (ARPA Order 2074) and is being monitored by Air Force Cambridge Research Laboratories.

This report may be reproduced to satisfy needs of U.S. Government agencies.

The views and conclusions contained in this document are those of the contractor and should not be interpreted as necessarily representing the official policies, either expressed or implied, of the Defense Advanced Research Projects Agency of the United States Government.

This technical report has been reviewed and is approved for publication.

FOR THE COMMANDER

Eugene C. Raabe
Eugene C. Raabe, Lt. Col., USAF
Chief, ESD Lincoln Laboratory Project Office

Non-Lincoln Recipients

PLEASE DO NOT RETURN

Permission is given to destroy this document
when it is no longer needed.

MASSACHUSETTS INSTITUTE OF TECHNOLOGY
LINCOLN LABORATORY

INTEGRATED OPTICAL CIRCUITS

SEMIANNUAL TECHNICAL SUMMARY REPORT
TO THE
ADVANCED RESEARCH PROJECTS AGENCY

1 JANUARY - 30 JUNE 1974

ISSUED 19 FEBRUARY 1975

Approved for public release; distribution unlimited.

LEXINGTON

MASSACHUSETTS

ABSTRACT

A detailed study has been made of electroabsorption avalanche photodiodes (EAP) fabricated in high-purity n-type epitaxial GaAs. These devices have their largest response at wavelengths beyond the usual absorption edge for high-purity materials. The absorption mechanism involves the Franz-Keldysh shift of the absorption edge, and the peak in response at the longer wavelengths can be explained by a much higher ionization coefficient for holes than for electrons. The results imply that the ratio of the coefficients β_p to α_n is even larger than previous measurements have given, and that GaAs avalanche diodes therefore have potentially wider bandwidth and lower noise capability than Si diodes. The electroabsorption effect opens up the attractive possibility of forming in high-purity GaAs waveguides detector as well as modulator elements.

The attenuation of high-purity planar GaAs waveguides has been examined at wavelengths close to the absorption edge. For wavelengths $> 9090 \text{ \AA}$, which can be obtained in Si-doped GaAs room-temperature lasers, the attenuation was found to be $\leq 1 \text{ cm}^{-1}$ in state-of-the-art epitaxial material.

The ability to selectively grow $Hg_{1-x}Cd_xTe$ on CdTe substrates by SiO_2 masking has been demonstrated using the hydrogen-transport epitaxial technique. This should eventually enable the fabrication of monolithic waveguide devices in this materials system, as well as various types of infrared detection and imaging devices.

Detailed measurements have been made of mode propagation at $10.6 \mu\text{m}$ in n/n^+ CdTe planar waveguides formed by proton bombardment. The waveguides are found to be highly uniform, reproducible, well characterized by a simple rectangular waveguide model and with low propagation losses determined by free-carrier absorption. Bragg-type acousto-optic modulators using Rayleigh surface acoustic waves have been fabricated in such n/n^+ CdTe waveguides and a modulation efficiency for $10.6\text{-}\mu\text{m}$ light of 10 percent has been obtained at 27 MHz with about 0.5 W of acoustic power.

High optical-quality planar waveguides have been fabricated in the $Pb_{1-x}Sn_xTe$ alloy system by molecular beam epitaxy. The structures consist of a $6\text{-}\mu\text{m}$ -thick low-carrier concentration ($\lesssim 4 \times 10^{16} \text{ cm}^{-3}$) $Pb_{0.92}Sn_{0.08}Te$ layer vacuum deposited on an n-type PbTe substrate followed by a second $0.5\text{-}\mu\text{m}$ -thick epitaxial layer of n-type PbTe. The measured propagation loss of $\leq 1.5 \text{ cm}^{-1}$ (6.5 dB/cm), for TE-polarized $10.6\text{-}\mu\text{m}$ laser radiation in these waveguides at 77 K, is sufficiently low for integrated optical circuits in this wavelength range; the waveguide fabrication techniques are compatible with those used for lasers and detectors in $Pb_{1-x}Sn_xTe$ epitaxial layers.

CONTENTS

Abstract	iii
I. GaAs-Based Integrated Optical Circuits	1
A. GaAs EAP Detectors	1
B. High-Purity GaAs Planar Waveguides	6
II. Hg _{1-x} Cd _x Te-CdTe Integrated Optical Circuits	7
A. Selective Epitaxial Deposition of Hg _{1-x} Cd _x Te	7
B. Mode Propagation Parameters of n/n ⁺ CdTe Waveguides	7
C. Integrated Bragg Acousto-Optic Modulator in an n/n ⁺ CdTe Waveguide at 10.6 μm	9
III. Lead-Salt Integrated Optical Circuits: Double Heterostructure Pb _{1-x} Sn _x Te Waveguides at 10.6 μm	11
References	14

INTEGRATED OPTICAL CIRCUITS

I. GaAs-BASED INTEGRATED OPTICAL CIRCUITS

A. GaAs EAP DETECTORS

In previous work on GaAs Schottky barrier avalanche photodiodes,¹ a slight increase in the response at longer wavelengths was observed for high reverse-bias voltages, and this increase was attributed mainly to the Franz-Keldysh² shift of the absorption edge. The effect observed was quite small, however, and the photo-response decreased monotonically for wavelengths longer than about 0.86 μm. In contrast, in the present work, the spectral response of the avalanche photodiodes (fabricated in the same way but on high-purity material) has a dominant peak in the 0.88- to 0.91-μm wavelength range. The variation of the spectral responsivity with bias voltage for an EAP detector fabricated on high-purity epitaxial material ($N_D - N_A \approx 5 \times 10^{14} \text{ cm}^{-3}$) with a thickness of about 20 μm is shown in Fig. 1. For this particular device, which has a breakdown voltage of 300 V, the depletion region reaches through to the substrate at about 200 V. However, the effect observed is not dependent on the reach-through structure. The spectral responsivity for 5-V reverse bias shown in Fig. 1(a) has a nearly constant quantum efficiency for wavelengths shorter than 0.87 μm and a sharp long wavelength cutoff starting at about 0.87 μm. As the bias voltage is increased, the long wavelength cutoff shifts to longer wavelengths and a peak develops in the response. Even at a bias voltage as low as 30 V, the external quantum efficiency at 0.88 μm exceeds unity because of avalanche gain. Figure 1(b) shows the spectral responsivity curves at still higher reverse-bias voltages. Similar results have been obtained on many different devices fabricated on other high-purity epitaxial material with $N_D - N_A$ in the 10^{14} - to 10^{15} cm^{-3} range. All the devices have essentially the same characteristics, whether or not the depletion width reaches through to the substrate before avalanche breakdown occurs. However, in devices fabricated on some material, the shoulder which is visible at about 0.90 μm on the peak in Fig. 1(a) is more pronounced, so that the peak response occurs at wavelengths as long as 0.91 μm. The spectral response for one such device is shown in Fig. 2. The net doping of the epitaxial layer for this device was less than $5 \times 10^{14} \text{ cm}^{-3}$ and the thickness of the layer was large enough so that the depletion region did not reach through to the substrate.

The increasing response with increasing bias voltage results from two effects: (1) increased response in this wavelength range due to electroabsorption, and (2) higher multiplication for the holes which are generated deeper in the high field region. The absorption mechanism for wavelengths longer than 0.88 μm involves the Franz-Keldysh effect on the absorption edge. Although the absorption which is related to the shoulder in Fig. 1 and the broader peak in Fig. 2 is not well understood at the present time, it probably involves the Franz-Keldysh effect and some shallow impurity level or defect center.

The absorption coefficient of a direct bandgap semiconductor in a uniform electric field E , for radiation of wavelength λ , can be expressed in mks units as³

$$\alpha(\lambda, E) = \frac{2^{7/3} \mu^{4/3} e^{7/3} |\bar{\epsilon} \cdot \bar{P}_{nn}| E^{1/3}}{\hbar^{8/3} \omega_m^2 n \epsilon_0 c} \int_{\beta}^{\infty} |Ai(z)|^2 dz . \quad (1)$$

In this equation $\beta = [(2\mu)^{1/3} (E_g - \hbar\omega)/(\hbar e E)^{2/3}]$, μ is the electron-hole reduced mass, e the electronic charge, \vec{E} the radiation polarization vector, $\bar{P}_{nn'}$ the usual zero-field interband matrix element, \hbar is Planck's constant/2 π , ω the frequency of the incident radiation of wavelength λ , m the free-electron mass, n the index of refraction, ϵ_0 the free-space dielectric constant, c the speed of light, and E_g the energy gap at zero field. The Airy functions, $Ai(z)$, are defined by

$$Ai(z) = \frac{1}{\pi} \int_0^\infty \cos\left(sz + \frac{s^3}{3}\right) ds . \quad (2)$$

The interband matrix element can be estimated using either the f-sum rule⁴ or the $\vec{k} \cdot \vec{p}$ band model.⁵ Using the f-sum rule, the interband matrix element can be written as

$$|P_{nn'}|^2 = \frac{1}{2} m\hbar\omega f_{nn'} \quad (3)$$

and the sum rule of the f's is

$$\sum f_{nn'} = 1 + \frac{m}{m_v} \quad (4)$$

where the sum is over direct transitions to all higher bands. Using Eqs. (3) and (4) and $f \approx 1 + m/m_v$, the Franz-Keldysh absorption coefficient for wavelengths close to the absorption edge can be written as

$$\alpha(\lambda, E) = 1.0 \times 10^4 \frac{f}{n} \left(\frac{2\mu}{m}\right)^{4/3} E^{1/3} \int_\beta^\infty |Ai(z)|^2 dz \quad (5)$$

where $\beta = 1.1 \times 10^5 (E_g - \hbar\omega)(2\mu/m)^{1/3} E^{-2/3}$, for α in cm^{-1} , E in V/cm , and $(E_g - \hbar\omega)$ in eV. In the calculations for GaAs that follow, the parameters that were used were $n = \text{constant} = 3.63$, $m_v/m = 0.087$ (since the light hole band gives the major contribution), and $\mu/m = 0.0377$, and the integral of the square of the Airy function was evaluated in terms of the Airy function and its derivative as

$$\int_\beta^\infty |Ai(z)|^2 dz = [\left| \left(\frac{dAi(z)}{dz} \right)_\beta \right|^2 + \beta |Ai(\beta)|^2] . \quad (6)$$

Equation (5) gives calculated values of α close to the band edge that are in good agreement with experiment. Alternatively, f or $P_{nn'}$ could have been treated as an adjustable parameter to obtain the same results.

Using Eq.(5), we can express the absorption coefficient at position x in the depletion region of a GaAs Schottky barrier or p^+ -n junction diode as $\alpha(\lambda, x)$ where the variation of electric field with position x , $E(x)$, is determined by the doping profile and applied bias voltage of the device considered. Then the generation rate of electron-hole pairs at position x in the depletion region for a given incident flux of photons of wavelength λ , $\varphi(\lambda)$, and sample reflectivity R , can be written as

$$G(\lambda, x) = \varphi(\lambda) (1 - R) g(\lambda, x) = \varphi(\lambda) (1 - R) \alpha(\lambda, x) \exp\left[-\int_0^x \alpha(\lambda, x') dx'\right] \quad (7)$$

with the assumption that each absorbed photon creates one electron-hole pair. The internal quantum efficiency of the detector for a given wavelength and applied voltage V , without avalanche gain, is then given by

$$\eta_o(\lambda, V) = \frac{\int_0^W G(\lambda, x) dx}{\varphi(\lambda)(1 - R)} = \int_0^W g(\lambda, x) dx = \int_0^W \alpha(\lambda, x) \exp\left[-\int_0^x \alpha(\lambda, x') dx'\right] dx \quad (8)$$

where W is the depletion width corresponding to the applied voltage V .

Equation (8) has been evaluated numerically, using a bandgap energy of 1.42 eV and the results for two different GaAs Schottky barrier devices with uniform doping profiles are shown in Fig. 3. The solid curves were calculated for a device on material with $N_D - N_A = 5 \times 10^{14} \text{ cm}^{-3}$ and the dashed curves were calculated for a device on material with $N_D - N_A = 2 \times 10^{16} \text{ cm}^{-3}$. For both doping levels, the internal quantum efficiency was evaluated at two different reverse-bias voltages: 0.05 and 0.90 of the corresponding breakdown voltage. There is a significant increase in the quantum efficiency of the more heavily doped device at the shorter wavelengths between the two bias levels. The increase is due to the widening of the depletion region as the bias voltage is increased and the resulting increased collection efficiency for the carriers generated at these wavelengths. At both bias levels, the long wavelength cutoff is more gradual for the device on $2 \times 10^{16} \text{ cm}^{-3}$ material, and this is due to the higher fields and larger Franz-Keldysh shift of the absorption edge in this material. However, the quantum efficiency is still low because, for this doping level, the depletion width even at avalanche breakdown is less than 2 μm . The gradual long wavelength cutoff is similar to that observed experimentally on devices of this doping level.¹ In contrast, at low bias voltages the device on high-purity material has a higher quantum efficiency at the shorter wavelengths and a much sharper long wavelength cutoff due, respectively, to the wider depletion region and lower electric fields in this device. At high reverse-bias voltages, the Franz-Keldysh effect becomes important and, along with the wider depletion region (about 30 μm at the breakdown voltage), results in a significant extension of the long wavelength cutoff for this device.

The results presented above show that the Franz-Keldysh effect in GaAs Schottky barrier detectors on high-purity material can result in an increase of the quantum efficiency to nearly unity at wavelengths which are beyond the long wavelength cutoff at low bias voltages. However, any increase above unity quantum efficiency must be due to avalanche multiplication.

For a Schottky barrier or p^+ -n detector with maximum electric field at $x = 0$ and zero electric field at $x = W$, the electron current increases with increasing x . The differential equation for the electron current $J_n(x)$ can be written as

$$\frac{dJ_n(x)}{dx} = \alpha_n(x) J_n(x) + \beta_p(x) J_p(x) + qG(x) \quad (9)$$

where α_n and β_p are the electron and hole ionization coefficients, respectively, $J_p(x)$ is the hole current and $G(x)$ is the generation rate of electron-hole pairs in the depletion region. The total current J is a constant so that

$$J = J_p(x) + J_n(x) = \text{constant} \quad , \quad (10)$$

and the differential equation for the hole current in the same device is

$$\frac{dJ_p(x)}{dx} = -\alpha_n(x) J_n(x) - \beta_p(x) J_p(x) - qG(x) \quad . \quad (11)$$

Considering only the space-charge generated photocurrent, these equations can be solved for the total current with the boundary conditions $J_n(0) = 0$ and $J_p(W) = 0$ and the internal device quantum efficiency with gain can be written as

$$\begin{aligned}\eta_1(\lambda, V) &= \frac{\int_0^W g(\lambda, x) \exp[-\int_0^x (\alpha_n - \beta_p) dx'] dx}{\{1 - \int_0^W \alpha_n \exp[-\int_0^x (\alpha_n - \beta_p) dx'] dx\}} \\ &= \frac{\exp[\int_0^W (\alpha_n - \beta_p) dx] \cdot \{\int_0^W g(\lambda, x) \exp[-\int_0^x (\alpha_n - \beta_p) dx'] dx\}}{\{1 - \int_0^W \beta_p \exp[\int_x^W (\alpha_n - \beta_p) dx'] dx\}} \quad (12)\end{aligned}$$

where $g(\lambda, x)$ is defined by Eq.(7). The device multiplication for a given wavelength and applied voltage is given by $M_o(V) = \eta_1(\lambda, V)/\eta_o(\lambda, V)$ and it can be seen that if $\alpha_n = \beta_p$, $M_o(\lambda, V)$ is independent of wavelength.

Equation (12) has been evaluated numerically for several different values of α_n and β_p for a device on material with a net donor concentration of $5 \times 10^{14} \text{ cm}^{-3}$ and the results are given in Fig. 4.

For Fig. 4(a), the values of the ionization coefficients obtained by Hall and Leck,⁶ $\alpha_n = \beta_p = 2.0 \times 10^5 \exp[-(5.5 \times 10^5/E)^2]$ were used and, as expected for the case where $\alpha_n = \beta_p$, the quantum efficiency is independent of wavelength out to the long wavelength cutoff, and the multiplication is constant for all wavelengths. The results are shown for applied voltages of 0.90, 0.95, 0.98 and 0.99 of the breakdown voltage of 496 V, determined using this ionization coefficient data. The value of the multiplication or internal quantum efficiency with gain is quite small and shows no resemblance to the experimental results in Figs. 1 or 2.

Figure 4(b) shows the calculated internal quantum efficiency with gain obtained from Eq.(12) for the case for $\beta_p > \alpha_n$, with $\alpha_n = 1.2 \times 10^7 \exp[-(2.3 \times 10^6/E)]$ and $\beta_p = 3.6 \times 10^8 \exp[-(2.9 \times 10^6/E)]$ from the data of Stillman, et al.⁷ The calculated breakdown voltage for this ionization coefficient data was 468 V and the calculated curves are shown for the same fractions of the breakdown voltage as in Fig. 4(a). These curves show a peak beginning to develop at the absorption edge similar to that observed experimentally, but the multiplication values obtained are still much too low. The quantum efficiency at the peak is too low relative to that at shorter wavelengths when compared with the experimental results.

The calculated internal quantum efficiency with gain for the ionization coefficients, which were arbitrarily adjusted to give agreement with the experimental breakdown voltages observed at low net donor concentrations, is shown in Fig. 4(c) for low applied voltages and in Fig. 4(d) for higher applied bias voltages. The ionization coefficients were $\alpha_n = 2 \times 10^6 \exp[-(2 \times 10^6/E)]$ and $\beta_p = 1 \times 10^5 \exp[-(5 \times 10^5/E)]$. The magnitude of the calculated quantum efficiency with gain, as well as the variation with both wavelength and bias voltage, are similar to that observed experimentally. Attempts to obtain more quantitative agreement are not warranted because of the limited accuracy of the absorption calculation. However, these results show that the experimental effect observed in the GaAs EAP detectors can be explained by electron and hole ionization coefficients which are consistent with the available breakdown voltage data and the previous conclusion that $\beta_p > \alpha_n$.

Since the response of the high-purity GaAs avalanche photodiodes at wavelengths beyond the absorption edge depends on a different mechanism than the response at wavelengths shorter than about 0.87 μm where the mechanism for absorption is the usual band-to-band absorption, the

response times for the two wavelength ranges are not necessarily the same. The Franz-Keldysh absorption at the wavelengths below the band edge is an electronic effect, however, and thus should not limit the bandwidth of the detectors.

The speed of response of the GaAs EAP detector whose spectral response is shown in Fig. 2 was evaluated using pulsed room-temperature GaAs lasers operating in a grating controlled external cavity.⁸ The response of one of these detectors with the laser operating at 0.92 μm is shown in Fig. 5(a) and the response of a Si avalanche photodiode to the same laser is shown in Fig. 5(b) for comparison. Both detectors were operated with a 50-ohm load. The structure in the first part of the pulse is actually present in the laser emission. The rise and fall times observed ($\lesssim 1$ nsec) are close to the limits imposed by the oscilloscope. The multiplication obtained with the GaAs EAP detector used for these measurements was limited by a relatively large series resistance which resulted from the undepleted high-purity GaAs. This high resistance causes a current saturation of the multiplication at high light levels. The 100-mV signal observed corresponds to a photocurrent of 2 mA and the multiplication obtained at this current level was about 20. At lower frequencies and photocurrents, gains of more than 200 were obtained so that with a properly designed detector operating at or near punch-through, an increase of at least a factor of ten in the detector signal should be obtained. The total response of the Si detector is nearly a factor of two larger than that of the GaAs detector, but the detected pulse is considerably distorted. This distortion probably results from the diffusion component of the photocurrent for the 0.92- μm radiation. The fast component of the Si detector response is smaller in amplitude than the GaAs detector response.

The limit of the frequency response of the GaAs EAP detectors could not be determined because of the lack of an adequate source in the 0.90- to 0.92- μm wavelength range. However, the response is probably not limited by the electroabsorption mechanism.

Although all the above discussion has been concerned with discrete EAP detectors, the electroabsorption effect is particularly promising for integrated waveguide photodetectors and modulators. High-purity GaAs and AlGaAs waveguides are being studied in many laboratories for use in near-infrared integrated optics and EAP detectors can be easily incorporated in these waveguides. With zero-bias voltage on a detector in such a waveguide, the radiation would pass through the detector with no absorption, but with a high reverse bias the light would be absorbed and detected with avalanche gain. For the power levels that will be used in integrated optical circuits, the Franz-Keldysh absorption mechanism can provide a fast and efficient modulator. The EAP device integrated in a waveguide should perform even better than the discrete devices. In this configuration the light will propagate parallel to the Schottky barrier contact or p-n junction and, thus, the effective absorption length can be much longer than the depletion layer width and waveguide thickness. Because of the intensity distribution of the light in the waveguide, the generation of electron-hole pairs should be more uniform and result in an even higher ratio of hole-to-electron injection and, therefore, lower noise than is obtained with the discrete device.

Seven of the discrete GaAs EAP detectors have been provided to the Naval Electronics Laboratory Center (NELC) for preliminary evaluation in fiber-optic communication and control systems. Work is in progress to fabricate more discrete EAP detectors, both Schottky barrier and p-n junction devices, with lower series resistance and higher avalanche gain at high current levels for NELC. Work is also under way to incorporate these detectors in two-dimensional high-purity GaAs waveguides.

G. E. Stillman J. A. Rossi
C. M. Wolfe J. P. Donnelly

B. HIGH-PURITY GaAs PLANAR WAVEGUIDES

The absorption of high-purity GaAs planar waveguides has been examined at wavelengths close to the absorption edge using a tunable GaAs room-temperature laser operating in a grating controlled external cavity. The preliminary measurements were made on a 20- μm -thick planar waveguide with $N_D - N_A \approx 10^{12}$ on an n^+ substrate with $N_D - N_A = 1 \times 10^{18}$. The measured absorption was equal to or less than 1 cm^{-1} for $\lambda \gtrsim 9090 \text{ \AA}$. At the wavelength of room-temperature GaAs lasers, 9050 \AA , the measured absorption was about 1.5 cm^{-1} and it increased to about 3 cm^{-1} for $\lambda = 9000 \text{ \AA}$. These results indicate that it may be possible to use these high-purity GaAs waveguides with GaAs room-temperature sources in integrated optical circuits. The losses of two-dimensional single-mode waveguides in this wavelength are currently under investigation.

G. E. Stillman
C. M. Wolfe
J. A. Rossi

II. $Hg_{1-x}Cd_xTe$ -CdTe INTEGRATED OPTICAL CIRCUITS

A. SELECTIVE EPITAXIAL DEPOSITION OF $Hg_{1-x}Cd_xTe$

Using the epitaxial growth reactor described previously,⁹ we have selectively grown $Hg_{1-x}Cd_xTe$ on CdTe through an SiO_2 mask by the process shown in Fig. 6. This process is very similar to that used for GaAs-In_{1-x}Ga_xAs monolithic waveguide detectors.⁹⁻¹¹ In Fig. 6(a) a pyrolytic SiO_2 is deposited on a single-crystal <100> CdTe substrate at a temperature of 500°C and circular regions are opened in the SiO_2 using standard photolithographic techniques. This patterned SiO_2 is then used as an etch mask and holes are etched in the CdTe substrate using a 0.02 Br:CH₃OH etchant to obtain the structure shown in Fig. 6(b). This etchant is non-preferential and the SiO_2 is undercut to about the same dimension as the hole depth. The structure shown in Fig. 6(b) is then placed in the epitaxial reactor, where the SiO_2 serves as a mask against growth. Thus, epitaxial growth of $Hg_{1-x}Cd_xTe$ is obtained only in the holes etched in the CdTe substrate to give the structure indicated in Fig. 6(c).

Figure 7 shows arrays of 125-μm-diameter regions of $Hg_{1-x}Cd_xTe$ which were grown out of 20-μm-deep holes in n⁺ CdTe substrates. The upper part of the figure shows the effect of substrate mis-orientation on this selective epitaxial hole growth. Although the CdTe substrate orientation is nominally <100>, the $Hg_{1-x}Cd_xTe$ hole growth facets exactly along <100>. Thus, the upper surface of the $Hg_{1-x}Cd_xTe$ regions is at an angle to the CdTe substrate. In the lower part of Fig. 7 the orientation of the CdTe substrate is much closer to <100> and the $Hg_{1-x}Cd_xTe$ facets are parallel to the substrate. In these experiments the $Hg_{1-x}Cd_xTe$ composition x was between 0.02 and 0.04. We expect that with improved control in the epitaxial reactor, selective epitaxial growth should be possible at the x = 0.20 composition appropriate for 10.6-μm detectors.

Grown-in regions similar to the above can be utilized as waveguide detectors if the surrounding CdTe is converted to high resistivity by proton bombardment.¹² With minor variations, this technique also can be used to fabricate other active and passive devices in a monolithic structure.

C. M. Wolfe

B. MODE PROPAGATION PARAMETERS OF n/n⁺ CdTe WAVEGUIDES

The TE₀ and TM₀ propagation loss in n/n⁺ CdTe waveguides fabricated by proton bombardment was found to be a strong function of guide layer thickness and in excellent agreement with absorption losses calculated for free-carrier absorption of the evanescent wave penetrating into the n⁺ substrate region.^{12,9} Using 2.5 × 2.5-mm sputter-etched grating couplers with a 5.08-μm periodicity to couple into higher-order waveguide modes, we have been able to measure the propagation constants and loss coefficients of each of the various TE and TM guide modes of several waveguides. The measured loss coefficients are again in excellent agreement with the above calculations. In addition, the propagation constants of the various modes are precisely those calculated assuming an abrupt refractive index change between the waveguide layer and n⁺ substrate.

The propagation constant of each waveguide mode was determined by the angle in which the CO₂ laser beam coupled into the waveguide when incident upon a grating coupler according to the relation

$$n_{\text{guide}} = \sin \theta + \frac{\lambda_0}{s}, \quad (13)$$

where n_{guide} is the effective index of the waveguide mode, θ is the angle of incidence, λ_o is the waveguide, and s the grating period. A very precise value of waveguide index is obtained in this manner as both λ_o and s (determined by the absolute precision of the pattern generator used to produce the photomask) are very accurately known. The coupling angle was measured to an accuracy of 0.1° , giving an absolute index accuracy of ± 0.001 . However, the angular separation between the coupling angle of two modes could be determined to about 0.02° , giving a relative index accuracy of ± 0.0002 .

The waveguide was mounted on a precision rotatable table with the input grating coupler at the axis of rotation. The radiation was collected from the cleaved face of the downstream end of the waveguide with an f/1 lens. In Fig. 8 is shown the radiation intensity emanating from the cleaved end face of a 28- μm -thick n/n⁺ CdTe waveguide as a function of incident angle for TE and TM polarizations. The two sets of recorder traces correspond to different input grating couplers on the same waveguide. In trace 1 the grating was about 1 mm from the end face, whereas in trace 2 the grating was 7.5 mm farther away. The coupling angle gives directly the effective index of the mode according to Eq. (13). The output intensity of each mode is a function of input intensity, coupling efficiency, and propagation loss. The propagation loss for each mode is obtained from the intensity ratio for the two grating distances, assuming both gratings have the same coupling efficiency. Upon examining several gratings fabricated simultaneously on the same waveguide, we find this to be a reasonable assumption. The magnitude of coupling efficiency can be obtained once the propagation loss is determined. For these particular forward coupled gratings excited from the air interface, we found the coupling efficiency to be about 3, 9, and 20 percent for the TM₀, TM₁, and TM₂ modes, respectively. The TE mode coupling was about one-half as efficient. More deeply etched gratings on thinner waveguides were much more efficient.⁹ The large increase in coupling efficiency with mode number is why the TE₁ and TE₂ mode output intensities are greater than that of the TE₀ mode in trace 1 where the coupler is near the end of the waveguide. Note the strikingly different intensity pattern in trace 2 where the grating is 7.5 mm farther upstream.

In Table I are listed the measured and theoretical waveguide propagation parameters for this 28- μm -thick n/n⁺ CdTe waveguide. The calculated effective index was obtained by assuming an abrupt index change between the proton-bombarded waveguiding layer and the n⁺ substrate. This assumption is justified on the basis of the well-defined range of high-energy protons and their relatively small straggling length.¹³ Since 10^{16} protons/cm² (i.e., $10^8/\mu\text{m}^2$) are needed to remove over 99 percent of the free carriers,¹² statistical variations in the waveguide layer thickness should be very small, much less than 1 μm .

On the basis of carrier removal studies on proton-bombarded CdTe, we expect the carrier concentration at the edge of the bombarded layer to drop from 90 percent down to 10 percent of the bulk concentration value within about 1/2 the straggling length. At 1.52 MeV the proton straggling length is about 0.7 μm . Thus, the diffuse region at the edge of the 28- μm -thick waveguiding layer should be about 0.4 μm or 1/10 of the 3.8- μm wavelength of CO₂ radiation in CdTe. The excellent agreement in Table I between the measured effective indices of the various modes and the values calculated on the basis of an abrupt index change bear out the above arguments. Similar comparisons of the measured and calculated effective indices on several other n/n⁺ CdTe waveguides of different thicknesses were made and found to be in equally good agreement. Thus, waveguides formed by proton bombardment to reduce the free-carrier effect on the dielectric constant can be described by a simple rectangular index profile just as well as the waveguides produced by evaporated layers.¹⁴

TABLE I
MEASURED AND THEORETICAL
 $\text{CdTe } n/n^+$ PLANAR WAVEGUIDE PROPAGATION PARAMETERS

Mode	Effective Index		Propagation Loss (dB/cm)	
	Measured	Calculated	Measured	Calculated ²
TE_a	2.6648	2.6649	3.1 ± 0.3	3.2
TE_1	2.6497	2.6498	11.5 ± 1	11.3
TE_2	2.6249	2.6251	26 ± 6	31
TE_3	—	2.5944		
TM_a	2.6644	2.6646	3.3 ± 0.3	3.3
TM_1	2.6491	2.6489	11.8 ± 0.5	11.8
TM_2	2.6240	2.6232	28 ± 5	34
Guide layer thickness	$28 \mu\text{m}$			
Material index	2.6706			
Laser wavelength	$10.27 \mu\text{m}$			
Substrate carrier concentration	$4.5 \times 10^{17}/\text{cm}^3$			
Residual guide layer carrier concentration	$4 \times 10^{15}/\text{cm}^3$			

Further verification of the validity of the rectangular profile is brought out by the close agreement between the measured and calculated propagation loss for each of the modes. The loss was calculated on the basis of free-carrier absorption in the substrate.⁹ The strong increase in attenuation with increasing mode number is due to the increasing amount of power in the evanescent tail penetrating into the heavily doped substrate and being attenuated by the free carriers.

In summary, we have found these n/n^+ CdTe waveguides to be highly uniform,⁹ reproducible, well characterized by a simple rectangular waveguide model and free-carrier absorption loss, but with very low loss for zero-order modes and predictably higher losses for higher-order modes.

D. L. Spears

C. INTEGRATED BRAGG ACOUSTO-OPTIC MODULATOR IN AN n/n^+ CdTe WAVEGUIDE AT $10.6 \mu\text{m}$

Bragg-type acousto-optic modulators using Rayleigh surface acoustic waves have been fabricated in n/n^+ CdTe optical waveguides. A modulation efficiency of 10 percent has been obtained at 27 MHz with about 0.5 W of acoustic power.

The Rayleigh waves were excited by 50.8- μm periodicity interdigital electrode transducers with 40 finger-pairs 2.5 mm long fabricated onto $\langle 111 \rangle$ CdTe coated with a 1- μm -thick layer of

sputtered ZnO. The ZnO was necessary to obtain a reasonable transducer conversion efficiency as the low electromechanical coupling constant of CdTe (Ref. 15) (6.8×10^{-4}) and the 2.5-mm transducer length give rise to a radiation impedance of less than 1 ohm for CdTe alone. Reactive sputtering in a partial pressure of oxygen necessary to deposit ZnO was found incompatible with a bare CdTe surface. To protect the CdTe, a 1500-Å layer of SiO₂ was pyrolytically deposited onto the CdTe before sputtering. Metal lift-off techniques were used to fabricate gold transducers onto the surface oriented along the <211> direction.

Examination of the transducers on an RF network analyzer revealed a peak radiation resistance of 3.5 ohms at 26.9 MHz with a bandwidth of 0.7 MHz. The surface wave velocity of 1.37×10^5 cm/sec deduced from this resonant frequency is in good agreement with that calculated from the CdTe elastic constants.¹⁶ Although the transducer radiation resistance was considerably higher than without the ZnO, it was only about one-half the expected value.¹⁷ The transducer bandwidth was limited by the large number of finger-pairs. Series resistance of 5 to 10 ohms in the gold fingers limited CW operation to less than 1 W of input electrical power.

A 21-μm-thick optical waveguiding layer was formed on the n⁺ CdTe by 1.31 MeV proton bombardment at room temperature either before or after the transducer fabrication. These waveguides have a TE₀ mode loss of about 5 dB/cm and their thickness closely matches the approximately 1/2-wavelength penetration of the 27-MHz Rayleigh waves. The modulator was evaluated by focusing a CO₂ laser beam onto the cleaved <110> end face of the waveguide and measuring the transmission modulation when an RF signal was applied to the transducer. A fast HgCdTe photodiode was used to detect the optical signal. Figure 9 shows the signal observed when an 18-W RF pulse was applied to the transducer. Over 8 percent of the radiation was scattered out of the optical beam by the acoustic waves. As much as 70 percent of this missing radiation has been collected by simply moving the detector to the Bragg angle. Figure 10 shows the modulation efficiency as a function of angle of incidence onto the cleaved <110> end face. The strong angular dependence is characteristic of Bragg scattering. The angle between the Stokes and anti-Stokes peaks is in excellent agreement with 11.6° calculated from the transducer periodicity. Slight transducer misalignment coupled with the strong beam-steering factor for this crystallographic orientation are most likely responsible for the fact that the pattern is not centered about normal incidence. The observed width of the two peaks is due to the large fractional bandwidth of Bragg diffraction at this low frequency, which is near the lower frequency limit of Bragg-type diffraction.¹⁸ In addition, when the incident laser beam was stopped down from f/20 to f/40 there was no significant increase in the peak modulation efficiency. From the measured modulation efficiency, we estimate the effective elasto-optic coefficient to be about 0.04. This is close in value to the shear wave coefficient, p₄₄, found for most materials. Since the Rayleigh surface wave has predominantly shear displacement, this similarity is to be expected.

Even at the highest power levels there was no indication of acoustic power saturation. The estimated maximum acoustic beam power of 0.5 W is about 1/3 of that required for strong non-linear effects to occur. With improved transducer design and fabrication, transducer conversion loss should be reduced to less than 3 dB, and CW acousto-optic modulation efficiencies could approach 50 percent.

D. L. Spears

III. LEAD-SALT INTEGRATED OPTICAL CIRCUITS: DOUBLE HETEROSTRUCTURE $Pb_{1-x}Sn_xTe$ WAVEGUIDES AT 10.6 μm

High optical-quality planar waveguides have been fabricated in $Pb_{1-x}Sn_xTe$ and waveguiding with losses sufficiently low for integrated optical circuit (IOC) applications has been observed at 77 K for 10.6- μm wavelengths. The heterostructure waveguides were formed by molecular beam epitaxy (MBE), which can be carried out at a sufficiently low temperature (400 °C) to produce low carrier concentration ($\lesssim 4 \times 10^{16} \text{ cm}^{-3}$) n-type $Pb_{1-x}Sn_xTe$ for the guiding layer. The guides consist of a 6- μm -thick $Pb_{0.92}Sn_{0.08}Te$ layer which is bounded on one side by an n-type PbTe substrate and on the other side by a 0.5- μm -thick epitaxial layer of n-type PbTe. Optical characterization of these guides indicates that the TE propagation loss is dominated by free-carrier absorption in the $Pb_{0.92}Sn_{0.08}Te$ guiding layer and at 77 K the loss coefficient is no greater than 1.5 cm^{-1} . This result lays the groundwork for fabricating monolithic IOC's in the lead salts by MBE, since this technique has already been used to fabricate lead-salt diode lasers¹⁹⁻²¹ and photodiodes^{22,23} in a way that is compatible with the waveguide fabrication.

The MBE technique used for the film growth is identical to that being employed in the fabrication of single²¹- and double²⁴-heterojunction $Pb_{1-x}Sn_xTe$ diode lasers. The structure of the waveguides is shown in Fig. 11. Substrate material was prepared by electrolytic etching of PbTe crystals which were vapor-grown²⁵ under metal-rich conditions. To test the compatibility of MBE layers with the photolithography required for the eventual fabrication of IOC's and to facilitate waveguide evaluation, the waveguides were fabricated as 125- μm -wide stripes using a lift-off technique. First, a 1500- \AA -thick SiO_2 layer was pyrolytically deposited on the substrate and 125- μm -wide stripes opened in the oxide by photolithographic techniques. The 6- μm -thick $Pb_{0.92}Sn_{0.08}Te$ and 0.5- μm -thick PbTe layers were then evaporated onto the substrates using undoped zone-melted single-crystalline Bridgman²⁶ material as the source material in an oil-free vacuum at approximately 10^{-7} -Torr pressure. The source furnaces were controlled to obtain a deposition rate of 1 μm /hour, with the substrate maintained at a 400 °C temperature by a radiant furnace.

For low foreign impurity densities, the n-type carrier concentrations of the films produced under these conditions cannot exceed the concentration determined by the metal-rich non-stoichiometric limit at the substrate temperature; hence, an upper limit of about $4 \times 10^{16} \text{ cm}^{-3}$ is expected for the guiding layer at 77 K (Ref. 26). Since the film growth over the oxide is amorphous and does not adhere well, these regions can be lifted off the substrate along with the oxide using a dilute solution of HF, leaving waveguide stripes. In order to protect the waveguides and to avoid optical leakage around the guides, the samples were plated with gold and indium on both sides and cold-bonded between opaque slabs of PbTe blocking material. The ends of the guides were then mechanically polished to obtain flat, parallel faces normal to the guide axis.

Analysis of a symmetric guide,²⁷ where the 6- μm $Pb_{0.92}Sn_{0.08}Te$ region with an estimated 77-K index of refraction^{28,29} of 6.32 is bounded by thick regions of PbTe on both sides with an index of 6.00, shows that three TE and three TM modes can propagate. It is to be expected, however, that a higher input-coupling efficiency and lower losses favor propagation in the fundamental modes.

Transmission measurements were made by focusing a CO₂ laser beam onto a polished guide end and detecting the total radiation emitted from the opposite end. By mechanically translating the polished sample face through the Gaussian laser spot, optical transmission scans (with resolution limited by the 22-μm half-power spot diameter) were obtained for the waveguide array and the substrate at both 300 and 77 K. Figure 12 is an optical scan made across one of the guides on a 4-mm-long substrate for both TE- and TM-polarized 10.6-μm radiation at 77 K. A strong peak in transmission is observed when the beam illuminates the input face of the guide. The broad, lower intensity background corresponds to unguided transmission when the PbTe substrate is illuminated. For the end-fire configuration used, the coupling losses are substantial and, in fact, transmission through the substrate is accentuated relative to the guide throughput by the approximately six-fold more efficient input/output coupling for the wide substrate compared to the narrow guide. At 300 K the TE transmission of these 4-mm-long guides is reduced by a factor of 21.3 ± 3.3 .

Since the laser scans do not represent near-field illumination patterns of the guide output face, measurements of far-field patterns were made to determine the order of the guided modes. Such patterns, observed for TE polarization at 300 K, consist of a single quasi-Gaussian lobe corresponding to propagation in the fundamental mode. The far-field pattern has about a 1-rad diffraction angle for full width at half power. This corresponds, in the Gaussian approximation, to a guide illumination with full width at half power of 4.3 μm and full width at $1/e^2$ power of 7.2 μm. As expected, the extent of the end-face illumination is about equal to a free-space wavelength which is essentially the minimum resolvable dimension. The field pattern, although at the resolution limit, appears to confirm that the 6-μm-thick Pb_{1-x}Sn_xTe layer is propagating effectively and radiating only the fundamental mode.

Transmission scans similar to those in Fig. 12 were obtained for TE polarization on an identical guide array which was polished to 1.25-mm length. Statistical analysis of the transmission through several guides (five of 4-mm length, and seven of 1.25-mm length) allows determination of the combined input and output coupling losses and of the waveguide attenuation at 300 and 77 K for TE modes with a good rms confidence level. The results are listed in Table II. Although at 77 K the TE propagation loss is too low to be determined accurately because of the short guide lengths in the experiment, an upper limit of 1.5 cm^{-1} (6.5 dB/cm) is estimated from the measurements.

The TE propagation loss measured at each temperature is in agreement with the estimated loss for free-carrier absorption. The carrier concentration of the guiding layer is somewhat uncertain. If the layer does not become metal saturated during growth, the carrier concentration at 77 K may be less than $4 \times 10^{16} \text{ cm}^{-3}$. In that case, the material could be intrinsic at 300 K with a total free-carrier concentration ($2n_i$) of 2 to $4 \times 10^{16} \text{ cm}^{-3}$ (Ref. 30). However, if the layer does reach metal saturation during growth, then at 77 K it should have an electron concentration of $4 \times 10^{16} \text{ cm}^{-3}$ and at 300 K a total free-carrier concentration ($n + p$) of 4.5 to $5.8 \times 10^{16} \text{ cm}^{-3}$. Assuming a 300 K mobility^{31,32} of about $1 \times 10^3 \text{ cm}^2/\text{V sec}$, the measured propagation loss of 7.8 cm^{-1} corresponds to a carrier concentration of $4 \times 10^{16} \text{ cm}^{-3}$ which, within the accuracy of this calculation, is consistent with either of the two cases above. For this concentration at 77 K, the maximum possible loss of 1.5 cm^{-1} corresponds to a mobility of $1.2 \times 10^4 \text{ cm}^2/\text{V sec}$, well within the range of measured mobility values for both MBE layers³² and bulk³³ Pb_{1-x}Sn_xTe. Since at 77 K either the layer concentration may be less than $4 \times 10^{16} \text{ cm}^{-3}$ or the mobility may be greater than $1.2 \times 10^4 \text{ cm}^2/\text{V sec}$, the actual free-carrier absorption loss may be substantially less than 1.5 cm^{-1} .

TABLE II
 $\text{PbTe}/\text{Pb}_{0.92}\text{Sn}_{0.08}\text{Te}/\text{PbTe}$ WAVEGUIDE RESULTS AT 10.6 μm

Propagation Loss (cm^{-1})			
	Guided Mode		Substrate
	TE_0	TM_0	TE/TM
77 K	<1.5	3.6 ± 1.4	7.9 ± 1.0
300 K	7.8 ± 1.4	16.4 ± 2.7	25 ± 2
End-Fire Coupling Efficiency (percent)			
Calculated	4.8	7.7	24
Measured	3.3 ± 1.6	-	20

Because transmission of TM-polarized radiation was measured only for the 4-mm-long waveguides, the coupling losses for TM modes have to be estimated from the known size of the input beam and the reflectivity at the input and output faces in order to determine the waveguide attenuation for TM modes. Such a plane wave estimate of the combined input and output coupling losses predicts maximum guide throughputs equal to the calculated coupling efficiencies listed in Table II. Since the calculated and measured values of the TE_0 coupling are in agreement, the calculated TM_0 coupling efficiency is presumed accurate. Note that the uncertainty in coupling caused by variations in the polishing of the guide end faces produces only a small uncertainty in the propagation loss coefficient.

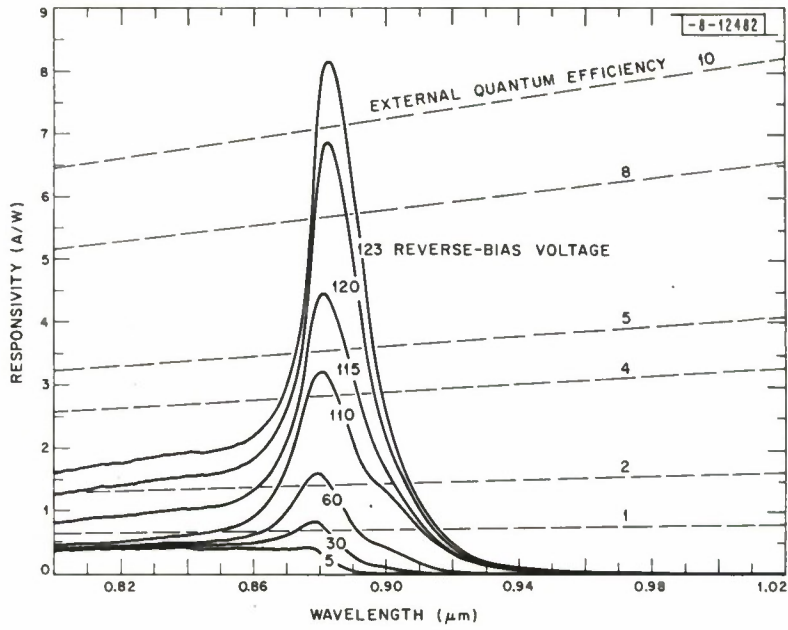
The higher TM attenuation can be qualitatively explained by losses associated with the metallic layer adjacent to the 0.5- μm PbTe cladding. For a symmetric guide consisting of a 6- μm $\text{Pb}_{0.92}\text{Sn}_{0.08}\text{Te}$ layer bounded on both sides by thick PbTe regions, the decay lengths³⁴ for both the TE_0 and TM_0 modes are approximately 0.9 μm ; hence, the evanescent fields appreciably penetrate the 0.5- μm -thick PbTe cladding and the effects of the adjacent metallic layer must be considered. Reisinger³⁵ has shown that the TM_0 differs in this case from the TM_{-1} mode of the symmetric guide and approaches the TM_{-1} mode (or surface plasmon mode) in the limit of zero thickness of the PbTe cladding. The TE_0 mode, however, does not change character with cladding thickness. For the present case of cladding thickness somewhat less than the decay length of the evanescent field, losses due to the metal can be shown to be insignificant for the TE_0 mode but appreciable for the TM_0 mode.^{35,36} The higher attenuation of TM modes in such a waveguide structure could be used to discriminate between the TM and TE modes in an IOC.

R. W. Ralston
J. N. Walpole
T. C. Harman

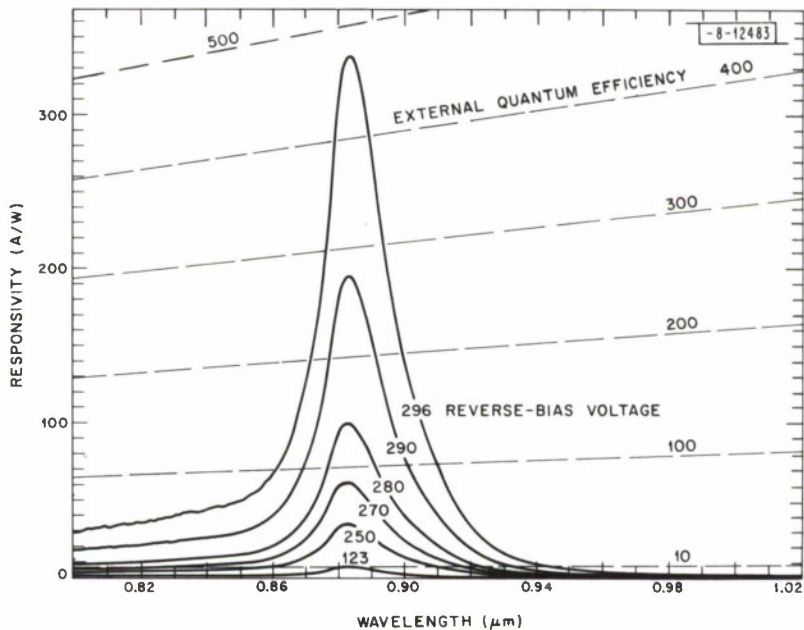
REFERENCES

1. W. T. Lindley, R. J. Phelan, Jr., C. M. Wolfe, and A. G. Foyt, *Appl. Phys. Lett.* 14, 197 (1969).
2. W. Franz, *Z. Naturforsch.* 13A, 494 (1958); L. V. Keldysh, *Sov. Phys.-JETP* 34, 788 (1958).
3. J. Callaway, *Phys. Rev.* 130, 549 (1963); 134, A998 (1964); see also K. Tharmalingham, *Phys. Rev.* 130, 2204 (1963).
4. J. Bardeen, F. J. Blatt, and L. H. Hall, in Photoconductivity Conference (Wiley, New York, 1956), p. 146.
5. J. Houghton and S. D. Smith, in Infrared Physics (Oxford University Press, London, 1966), p. 131.
6. R. Hall and J. H. Leck, *Int. J. Electronics* 25, 529 (1968).
7. G. E. Stillman, C. M. Wolfe, J. A. Rossi, and A. G. Foyt, *Appl. Phys. Lett.* 24, 471 (1974).
8. J. A. Rossi, S. R. Chinn, and H. Heckscher, *Appl. Phys. Lett.* 23, 25 (1973).
9. Integrated Optical Circuits Semiannual Technical Summary, Lincoln Laboratory, M.I.T. (31 December 1973), p. 5, DDC AD-781102/9.
10. G. E. Stillman, C. M. Wolfe, and I. Melngailis, *Appl. Phys. Lett.* 25, 36 (1974).
11. C. M. Wolfe, G. E. Stillman, and I. Melngailis, *J. Electrochem. Soc.* 121, 1506 (1974).
12. Integrated Optical Circuits Semiannual Technical Summary, Lincoln Laboratory, M.I.T. (31 July 1973), p. 5, DDC AD-769858/2.
13. J. F. Janni, Air Force Weapons Laboratory Technical Report No. AFWL-TR-65-150 (September 1966).
14. P. K. Tien, R. Ulrich, and R. J. Martin, *Appl. Phys. Lett.* 14, 291 (1969).
15. D. A. Berlincourt, H. Jaffe, and L. R. Shiozawa, *Phys. Rev.* 192, 1009 (1963).
16. H. J. McSkimin and D. G. Thomas, *J. Appl. Phys.* 33, 56 (1962).
17. G. S. Kino and R. S. Wagers, *J. Appl. Phys.* 44, 1480 (1973).
18. N. Uchida and N. Niizeki, *Proc. IEEE* 61, 1073 (1973).
19. H. Holloway, W. H. Weber, E. M. Logothetis, A. J. Varga, and K. F. Yeung, *Appl. Phys. Lett.* 21, 5 (1972).
20. W. H. Weber and K. F. Yeung, *J. Appl. Phys.* 44, 4991 (1973).
21. J. N. Walpole, A. R. Calawa, R. W. Ralston, T. C. Harman, and J. P. McVittie, *Appl. Phys. Lett.* 23, 620 (1973).
22. E. M. Logothetis, H. Holloway, A. J. Varga, and E. Wilkes, *Appl. Phys. Lett.* 19, 318 (1971).
23. J. P. Donnelly and H. Holloway, *Appl. Phys. Lett.* 23, 682 (1973).
24. J. N. Walpole, R. W. Ralston, A. R. Calawa, and T. C. Harman, to be published in Proceedings of the Fourth Int. IEEE Semiconductor Laser Conference, Atlanta, Georgia, November 1974.
25. T. C. Harman and J. P. McVittie, *J. Electron. Mater.* 3, 843 (1974).
26. T. C. Harman, *J. Nonmetals* 1, 183 (1973).
27. P. K. Tien, *Appl. Opt.* 10, 2395 (1971).
28. J. N. Zemel, J. D. Jensen, and R. B. Scholar, *Phys. Rev.* 140, A330 (1965).
29. G. F. Dionne and J. C. Wooley, *Phys. Rev. B* 6, 3898 (1972).

30. I. Melngailis and T. C. Harman, in Semiconductors and Semimetals, Vol. V, R.W. Willardson and A.C. Beer, Eds. (Academic Press, New York, 1970), p. 159. In the calculations of the intrinsic carrier concentration and the free-carrier absorption, the effective masses of $\text{Pb}_{0.92}\text{Sn}_{0.08}\text{Te}$ are assumed to scale with energy gap from the band-edge values determined for PbTe at 4.2 K. Thus, the density-of-states and conductivity effective masses are $0.7 m_0 E_g$ and $0.18 m_0 E_g$, respectively, with E_g (300 K) = 0.256 eV and E_g (77 K) = 0.159 eV.
31. The mobility for n-type bulk PbTe at 300 K has been determined as $1.5 \times 10^3 \text{ cm}^2/\text{V sec}$ by A. J. Strauss, *J. Nonmetals* 1, 133 (1973).
32. The mobility of 4 to $6 \times 10^{16} \text{ cm}^{-3}$ n-type MBE layers of PbTe and $\text{Pb}_{0.80}\text{Sn}_{0.20}\text{Te}$ has been determined by H. Holloway and E. M. Logothetis, *J. Appl. Phys.* 42, 4522 (1971). Approximate values are 1×10^3 and $3 \times 10^4 \text{ cm}^2/\text{V sec}$ at 300 and 77 K, respectively.
33. A. R. Calawa, T. C. Harman, M. C. Finn, and P. Youtz, *Trans. Met. Soc. AIME* 242, 374 (1968).
34. H. Kogelnik and V. Ramaswamy, *Appl. Opt.* 13, 1857 (1974).
35. A. Reisinger, *Appl. Opt.* 12, 1015 (1973).
36. W.H. Weber, S. L. McCarthy, and M. Mikkor, IOC Final Technical Report (February 1974), Ford Motor Company, ARPA Order 2327 (unpublished).

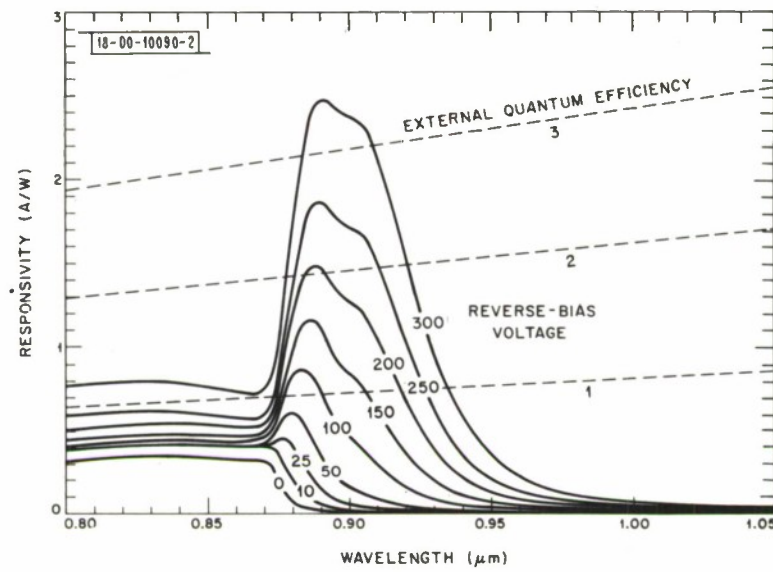


(a)

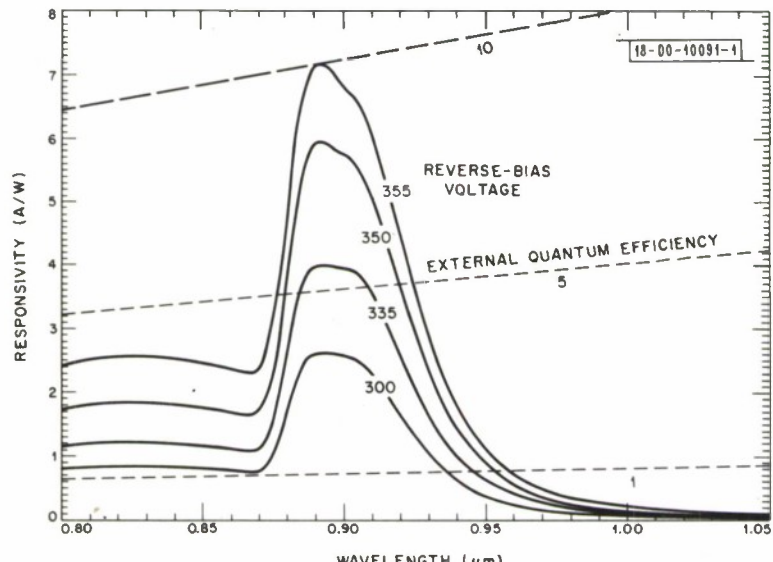


(b)

Fig. 1. Experimental variation of spectral response with reverse-bias voltage for a GaAs Schottky barrier EAP detector for (a) low voltages and (b) high voltages. The epitaxial material was about 20 μm thick and had a net donor concentration of about $5 \times 10^{14} \text{ cm}^{-3}$.



(a)



(b)

Fig. 2. Variation of spectral response with bias voltage for a GaAs avalanche photodiode fabricated on different material with $N_D - N_A \lesssim 5 \times 10^{14} \text{ cm}^{-3}$.

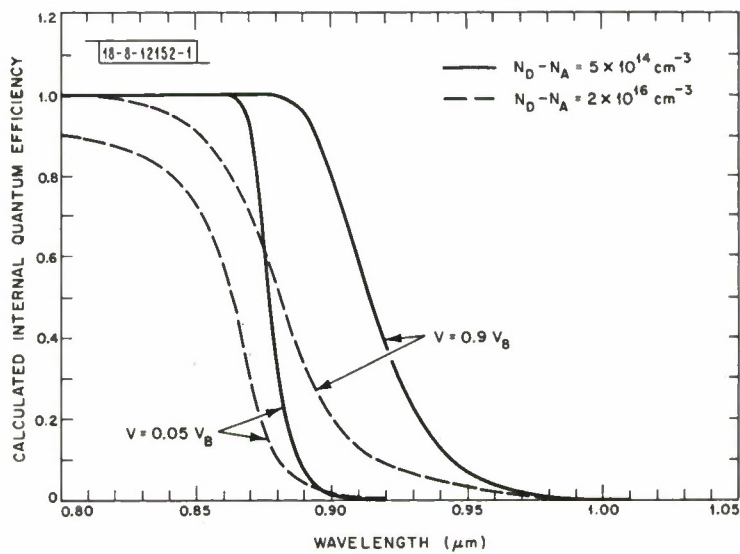


Fig. 3. Calculated internal quantum efficiency for two Schottky barrier diodes with $N_D - N_A = 5 \times 10^{14}$ and $2 \times 10^{16} \text{ cm}^{-3}$, respectively. The calculations were done at applied voltages of 0.05 and 0.9 of the corresponding breakdown voltages for the case of no multiplication of avalanche gain, but including the Franz-Keldysh electroabsorption.

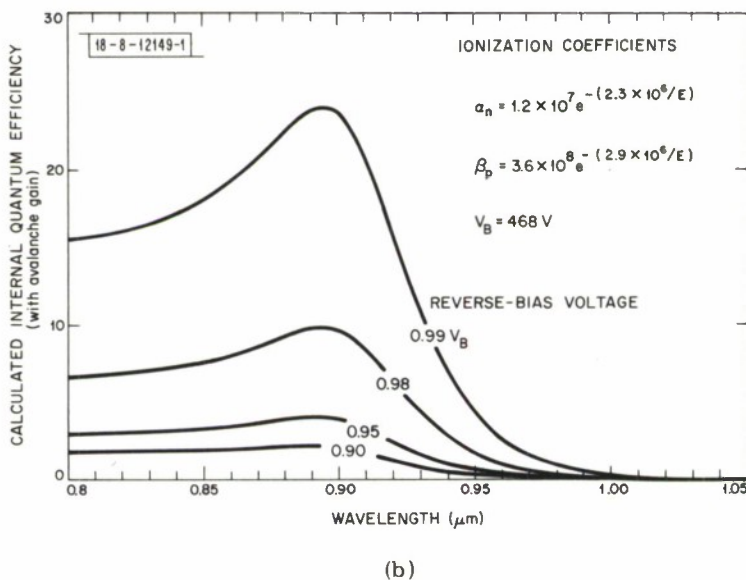
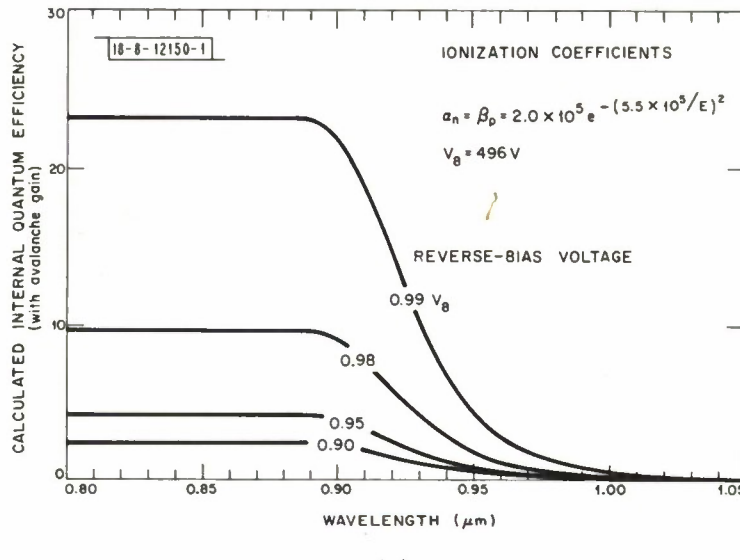
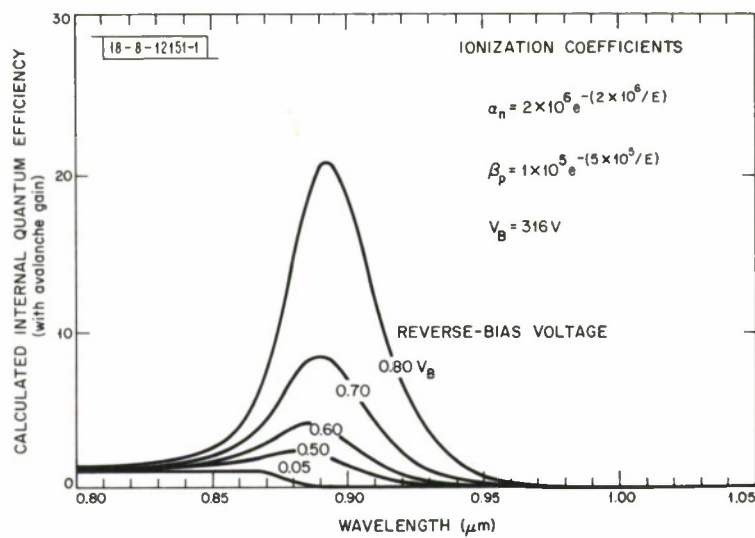
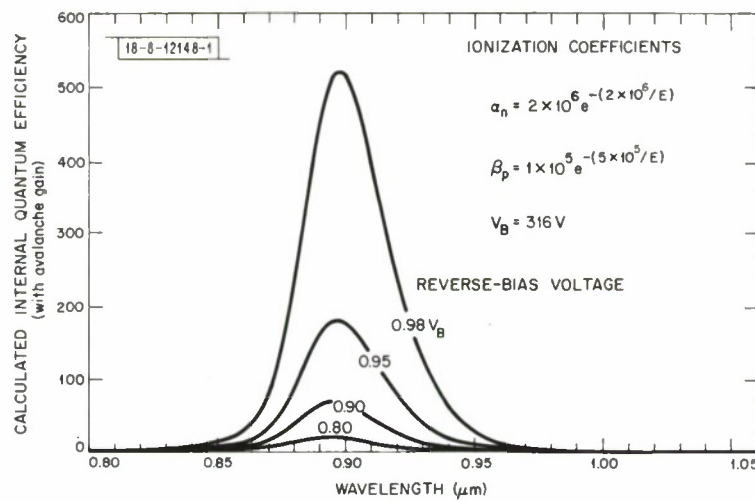


Fig. 4. Calculated internal quantum efficiency with gain for a GaAs EAP detector on uniformly doped material with $N_D - N_A = 5 \times 10^4 \text{ cm}^{-3}$, for three different sets of ionization coefficient data, as indicated in the figures. In each case the breakdown voltage determined for the ionization coefficients is shown and the spectral quantum efficiency curves were calculated for the given fractions of the corresponding breakdown voltages. (a) Ionization coefficients of Hall and Leck (1969), (b) ionization coefficient data of Stillman, *et al.* (1974b), (c) and (d) ionization coefficients adjusted to obtain agreement with reported values of breakdown voltage on lightly doped material.

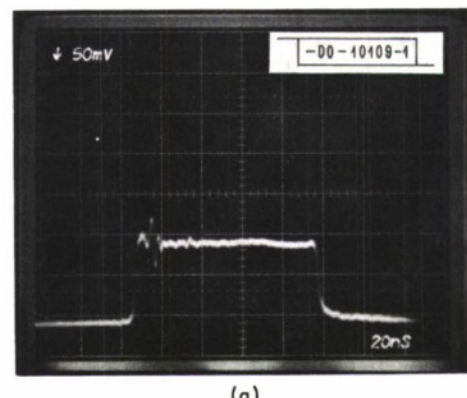


(c)

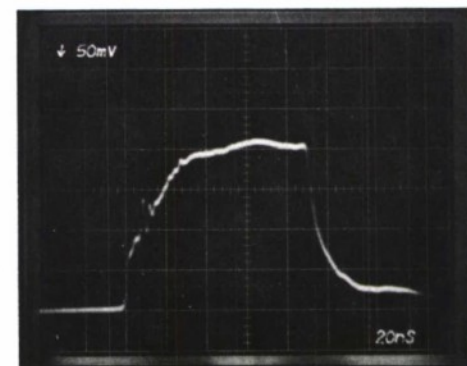


(d)

Fig. 4. Continued.



(a)



(b)

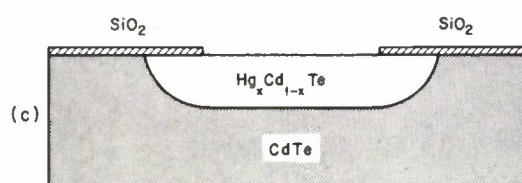
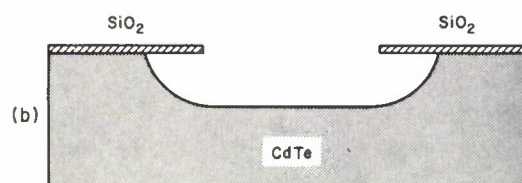
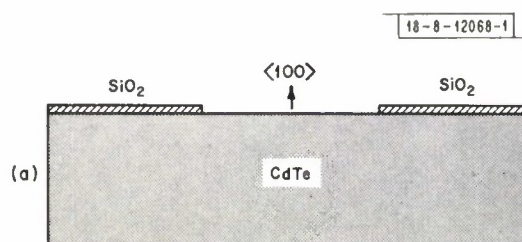


Fig. 6. Selective epitaxial deposition process for the growth of HgCdTe regions in CdTe substrates.

-8-11801-1

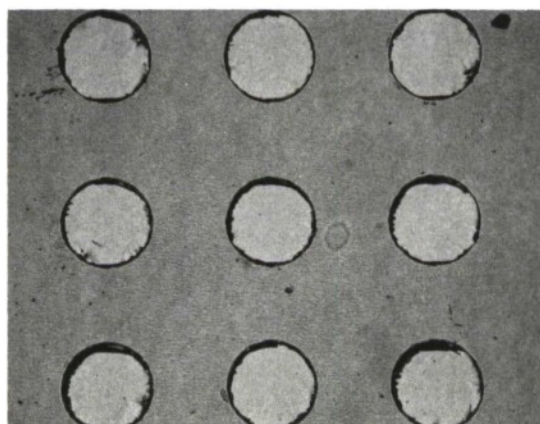
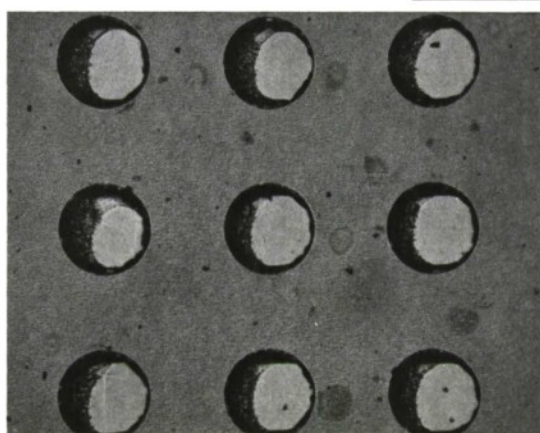


Fig. 7. Circular regions of $\text{Hg}_{1-x}\text{Cd}_x\text{Te}$, 125 μm in diameter, 20 μm deep, grown in CdTe substrates: upper part, substrate orientation nominally $\langle 100 \rangle$; lower part, substrate orientation $\langle 100 \rangle$.

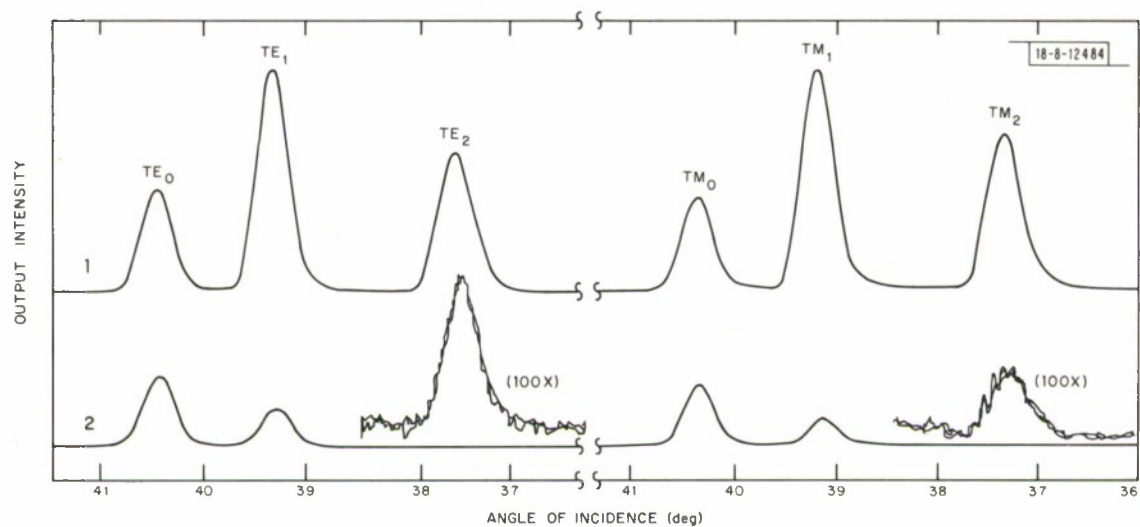


Fig. 8. CO_2 laser output intensity from the end of a n/n^+ CdTe waveguide as a function of angle of incidence onto a 2.5-mm-square grating coupler: trace 1, 1 mm from the end; trace 2, 8.5 mm from the end.

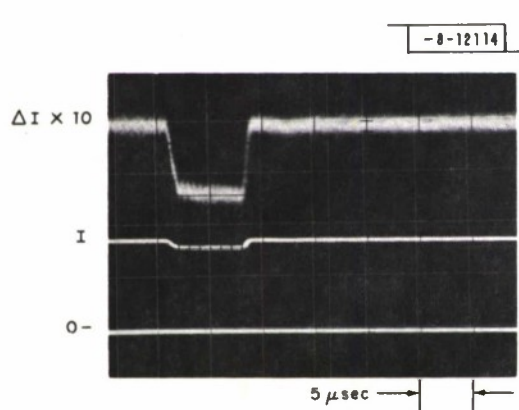


Fig. 9. Oscilloscope display showing the modulation of a 10.6- μm optical beam in a CdTe waveguide produced by 27-MHz acoustic surface waves.

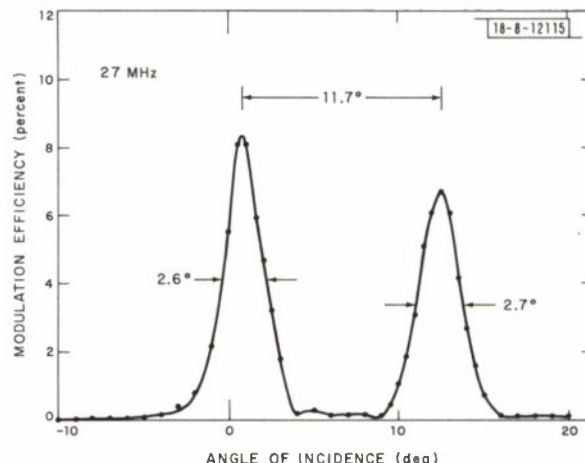


Fig. 10. Modulation efficiency of a 10.6- μm CdTe waveguide acousto-optic modulator as a function of the incident angle of the optical beam.

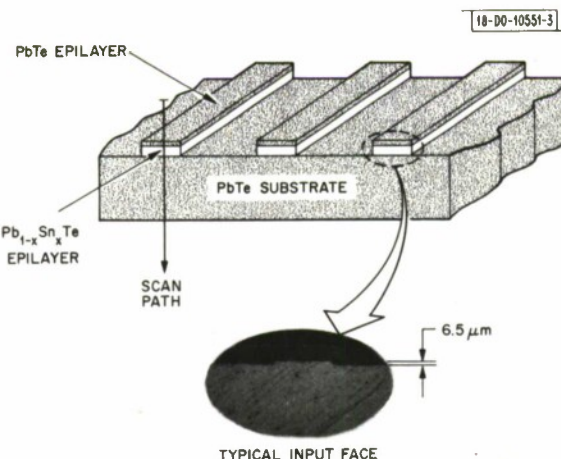


Fig. 11. Double heterostructure lead-salt waveguide configuration. Each guide is a 125- μm -wide stripe consisting of a 6- μm -thick layer of $\text{Pb}_{0.92}\text{Sn}_{0.08}\text{Te}$ covered by a 0.5- μm -thick layer of PbTe. Note the scan path for subsequent optical characterization.

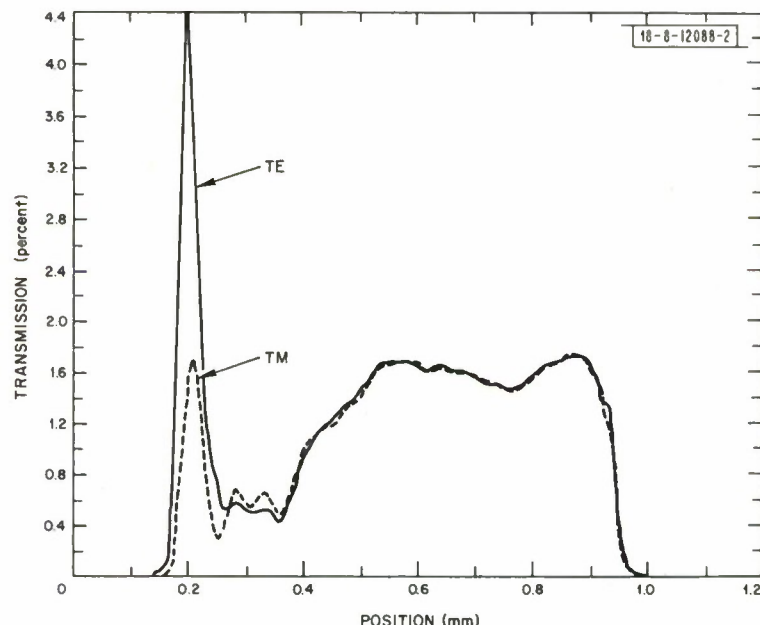


Fig. 12. Transmission scans of TE- and TM-polarized 10.6- μm laser beams along the path indicated in Fig. 11 for a 4-mm-long $\text{Pb}_{0.92}\text{Sn}_{0.08}\text{Te}$ -PbTe double heterostructure waveguide at 77 K. Loss due to coupling is estimated at 95.2 and 92.3 percent for the TE_0 and TM_0 modes, respectively. The guiding layer is located at the 0.2-mm position, the entire sample is 0.75 mm thick.

UNCLASSIFIED

SECURITY CLASSIFICATION OF THIS PAGE (When Data Entered)

REPORT DOCUMENTATION PAGE		READ INSTRUCTIONS BEFORE COMPLETING FORM												
1. REPORT NUMBER ESD-TR-75-103	2. GOVT ACCESSION NO.	3. RECIPIENT'S CATALOG NUMBER												
4. TITLE (and Subtitle) Integrated Optical Circuits		5. TYPE OF REPORT & PERIOD COVERED Semiannual Technical Summary 1 January - 30 June 1974												
		6. PERFORMING ORG. REPORT NUMBER												
7. AUTHOR(s) Melngailis, Ivars		8. CONTRACT OR GRANT NUMBER(s) F19628-73-C-0002												
9. PERFORMING ORGANIZATION NAME AND ADDRESS Lincoln Laboratory, M.I.T. P.O. Box 73 Lexington, MA 02173		10. PROGRAM ELEMENT, PROJECT, TASK AREA & WORK UNIT NUMBERS ARPA Order 2074												
11. CONTROLLING OFFICE NAME AND ADDRESS Advanced Research Projects Agency 1400 Wilson Boulevard Arlington, VA 22209		12. REPORT DATE 30 June 1974												
		13. NUMBER OF PAGES 32												
14. MONITORING AGENCY NAME & ADDRESS (if different from Controlling Office) Air Force Cambridge Research Laboratories Hanscom AFB Bedford, MA 01731		15. SECURITY CLASS. (of this report) Unclassified												
		15a. DECLASSIFICATION DOWNGRADING SCHEDULE												
16. DISTRIBUTION STATEMENT (of this Report) Approved for public release; distribution unlimited.														
17. DISTRIBUTION STATEMENT (of the abstract entered in Block 20, if different from Report)														
18. SUPPLEMENTARY NOTES None														
19. KEY WORDS (Continue on reverse side if necessary and identify by block number) <table style="width: 100%; border-collapse: collapse;"> <tr> <td style="width: 33%;">Integrated Optical Circuits</td> <td style="width: 33%;">heterodyne detection</td> <td style="width: 33%;">proton bombardment</td> </tr> <tr> <td>electroabsorption effect</td> <td>avalanche photodiodes</td> <td>$Hg_{1-x}Cd_xTe$-CdTe</td> </tr> <tr> <td>GaAs</td> <td>acoustic waves</td> <td>$Pb_{1-x}Sn_xTe$</td> </tr> <tr> <td>epitaxial growth</td> <td>Schottky barrier</td> <td></td> </tr> </table>			Integrated Optical Circuits	heterodyne detection	proton bombardment	electroabsorption effect	avalanche photodiodes	$Hg_{1-x}Cd_xTe$ -CdTe	GaAs	acoustic waves	$Pb_{1-x}Sn_xTe$	epitaxial growth	Schottky barrier	
Integrated Optical Circuits	heterodyne detection	proton bombardment												
electroabsorption effect	avalanche photodiodes	$Hg_{1-x}Cd_xTe$ -CdTe												
GaAs	acoustic waves	$Pb_{1-x}Sn_xTe$												
epitaxial growth	Schottky barrier													
20. ABSTRACT (Continue on reverse side if necessary and identify by block number) <p>A detailed study has been made of electroabsorption avalanche photodiodes (EAP) fabricated in high-purity n-type epitaxial GaAs, and the attenuation of high-purity planar GaAs waveguides has been examined at wavelengths close to the absorption edge. The results open up the attractive possibility of forming in high-purity GaAs waveguides detector as well as modulator elements based on the electroabsorption effect.</p> <p>The ability to selectively grow $Hg_{1-x}Cd_xTe$ on CdTe substrates by SiO_2 masking has been demonstrated using the hydrogen-transport epitaxial technique.</p> <p>Detailed measurements have been made of mode propagation at 10.6 μm in n/n⁺ CdTe planar waveguides formed by proton bombardment. Bragg-type acousto-optic modulators using Rayleigh</p>														

20. ABSTRACT (Continued)

surface acoustic waves have been fabricated in such n/n⁺ CdTe waveguides and a modulation efficiency for 10.6-μm light of 10 percent has been obtained at 27 MHz with about 0.5 W of acoustic power.

Planar waveguides with propagation losses $\leq 1.5 \text{ cm}^{-1}$ (6.5 dB/cm) at 10.6-μm wavelength have been fabricated in the Pb_{1-x}Sn_xTe alloy system for eventual use in integrated 10.6-μm heterodyne receivers.